Zhao et al. *NPG Asia Materials* (2023) 15:71
https://doi.org/10.1038/s41427-023-00517-5

NPG Asia Materials

ARTICLE Open Access

Design of ohmic contacts between Janus MoSSe and two-dimensional metals

Ning Zhao[1], Shubham Tyagi[1] and Udo Schwingenschlögl[1]

Abstract

Two-dimensional semiconductors are considered as channel materials for field-effect transistors to overcome short-channel effects and reduce the device size. As the contacts to the metallic electrodes are decisive for the device performance, we study the electronic properties of contacts between Janus MoSSe and various two-dimensional metals. We demonstrate that weak interactions at these van der Waals contacts suppress Fermi level pinning and show that ohmic contacts can be formed for both terminations of Janus MoSSe, generating favorable transport characteristics.

Introduction

Over the past decades, the performance of silicon as a channel material for field-effect transistors has reached a limit. Due to short channel effects at scales below 3 nm and further bottlenecks, alternative channel materials need to be explored[1–5]. Due to their high stability[6,7] and suitable band gap[8], two-dimensional (2D) transition-metal dichalcogenides are of particular interest[9,10]. The family of 2D transition-metal dichalcogenides also comprises Janus materials[11], such as MoSSe, which are special because their structural asymmetry introduces an electric dipole[12,13]. This dipole may affect the contacts between the channel material and metallic electrodes, which are critical for the device performance[14,15].

To achieve an ohmic contact, the barrier height of a Schottky semiconductor-metal contact is commonly regulated to zero by selecting a metal with an appropriate work function[16]. Regrettably, Fermi level pinning hinders this regulation and thus compromises electron transport[17]. Bulk metals often generate metal-induced gap states[18] and strong contact interactions due to dangling bonds[19], which both enhance Fermi level pinning[20]. To address these issues, the thickness of the metal can be reduced to the nanoscale[21,22], and buffer layers can be added[23,24]. Alternatively, the semiconductor can be placed in contact with a 2D metal[25–30] to form weakly interacting van der Waals contacts and simultaneously reduce the device size[31–33]. However, it is not known how the electric dipole of a Janus semiconductor employed as a channel material influences the properties of van der Waals contacts. For this reason, we study the electronic properties of contacts formed between Janus MoSSe and 2D metals. In particular, we demonstrate suppression of the Fermi level pinning and formation of ideal ohmic contacts.

Computational methods

All calculations are performed using the projector-augmented wave method of the Vienna ab initio simulation package[34] with a 500 eV plane wave energy cutoff. A dipole correction is added for each of the studied systems. The optB88-vdW functional is adopted to accurately model the van der Waals interaction[35,36], as it reliably describes 2D layered systems[37]. The band structure and work function are evaluated using the hybrid Heyd-Scuseria-Ernzerhof functional[38]. We set the convergence criteria to 10^{-5} eV for the total energy and to 0.01 eV/Å for the maximal residual force. Vacuum layers of 20 Å thickness are added to the structure models to ensure that artificial interaction does not occur in the out-of-plane direction due to the periodic boundary conditions. A Monkhorst-Pack k-grid with a separation of 0.015 to 0.020 Å^{-1} between the grid points is employed. Electronic

Correspondence: Udo Schwingenschlögl (udo.schwingenschlogl@kaust.edu.sa)
[1]Applied Physics Program, Physical Science and Engineering Division, King Abdullah University of Science and Technology (KAUST), Thuwal 23955-6900, Saudi Arabia

© The Author(s) 2023

Open Access This article is licensed under a Creative Commons Attribution 4.0 International License, which permits use, sharing, adaptation, distribution and reproduction in any medium or format, as long as you give appropriate credit to the original author(s) and the source, provide a link to the Creative Commons license, and indicate if changes were made. The images or other third party material in this article are included in the article's Creative Commons license, unless indicated otherwise in a credit line to the material. If material is not included in the article's Creative Commons license and your intended use is not permitted by statutory regulation or exceeds the permitted use, you will need to obtain permission directly from the copyright holder. To view a copy of this license, visit http://creativecommons.org/licenses/by/4.0/.

transport calculations are performed using the none-quilibrium Green's function method of the Quantum ATK package[39] with norm-conserving pseudopotentials (300 Ry energy cutoff). A Monkhorst-Pack 1 × 5 × 100 k-grid is employed for the semi-infinite electrode calculations, and a Monkhorst-Pack 1 × 5 × 1 k-grid is employed for the transport calculations.

We study graphene and silicene as classical group-IV 2D metals and M_3C_2 (M = Zn, Cd, Hg) as a new class of promising 2D Dirac metals[40]. Based on the structure of MoSSe, we further select metallic 1T- and 2H-phase transition-metal dichalcogenides XA_2 with X = Nb, Ta and A = S, Se, Te. The unit cells of all the 2D metals are presented in Fig. 1. Contacts between the S- and Se-sides of MoSSe with the 2D metals are considered, which are referred to as SeMoS/metal and SMoSe/metal contacts, respectively. The in-plane lattice constants of the contact structure models are set to the average of the component's lattice constants, and the lattice mismatch is minimized by the following supercells (remaining lattice mismatch given in brackets): √7 × √7 × 1 graphene (0.4%), √3 × √3 × 1 silicene (3.3%), and 1 × 1 × 1 Zn_3C_2 (0.1%) on 2 × 2 × 1 MoSSe; √3 × √3 × 1 Cd_3C_2 (4.6%) and √3 × √3 × 1 Hg_3C_2 (5.6%) on 4 × 4 × 1 MoSSe; 1 × 1 × 1 NbS_2 (2H: 3.0%), $NbSe_2$ (2H: 6.8%), TaS_2 (1T: 3.9%; 2H: 2.8%), and $TaSe_2$ (2H: 6.6%) on 1 × 1 × 1 MoSSe; √7 × √7 × 1 $TaTe_2$ (1T: 0.3%; 2H: 0.6%) on 3 × 3 × 1 MoSSe.

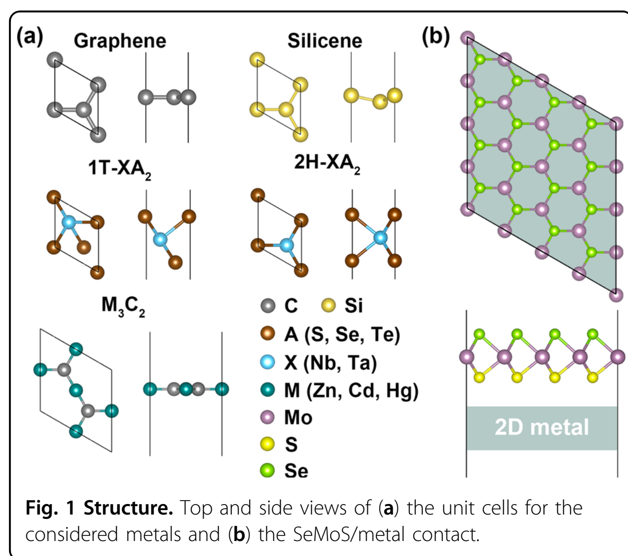

Fig. 1 Structure. Top and side views of (**a**) the unit cells for the considered metals and (**b**) the SeMoS/metal contact.

Results and discussion

Due to the asymmetry of Janus MoSSe, the properties of both the S- and Se-sides are examined. The binding energy of a contact is calculated as $E_b = (E_{contact} - E_{MoSSe} - E_{metal})/A$, where $E_{contact}$, E_{MoSSe}, and E_{metal} are the total energies of the contact, isolated MoSSe, and isolated metal, respectively. Moreover, A is the contact area, which is used for normalization. For each contact, the obtained values of E_b and the interlayer spacing d are shown in Table 1. For contacts with both the S- and Se-sides, E_b is highest for XA_2 (except for $TaTe_2$), intermediate for group-IV 2D metals, and lowest for M_3C_2. For group-IV 2D metals and M_3C_2, the S-side provides a higher E_b than

Table 1 Absolute binding energy ($|E_b|$), contact spacing (d), charge transfer across the contact (Δq), and n/p-type Schottky barrier height (Φ_n/Φ_p) of SeMoS/metal and SMoSe/metal contacts.

Metal	SeMoS/metal					SMoSe/metal				
	$\lvert E_b\rvert$ (J/m^2)	d (Å)	Δq (×10^{-3} e/Å^2)	Φ_n (eV)	Φ_p (eV)	$\lvert E_b\rvert$ (J/m^2)	d (Å)	Δq (×10^{-3} e/Å^2)	Φ_n (eV)	Φ_p (eV)
Graphene	0.35	3.33	0.4	0.19		0.35	3.49	−0.1	0.80	
Silicene	0.37	3.12	4.5	0.10		0.36	3.31	2.9	0.55	
Zn_3C_2	0.26	3.06	3.3			0.25	3.14	1.6		
Cd_3C_2	0.27	3.16	3.3			0.25	3.34	2.1		
Hg_3C_2	0.25	3.30	1.6			0.24	3.46	0.9		
2H-NbS_2	0.44	2.94	−1.5		0.51	0.46	3.03	−3.8		0.08
2H-$NbSe_2$	0.44	3.00	−0.2	0.44		0.44	3.09	−1.2		0.31
1T-TaS_2	0.43	2.91	−0.7	0.09		0.42	3.07	−1.8	0.66	
2H-TaS_2	0.40	2.96	−1.0		0.37	0.41	3.05	−3.1		
2H-$TaSe_2$	0.43	3.03	0.1	0.30		0.43	3.09	−0.9		0.45
1T-$TaTe_2$	0.35	3.40	2.1	0.26		0.34	3.54	1.2	0.89	
2H-$TaTe_2$	0.35	3.40	1.7	0.62		0.36	3.51	0.9		0.94

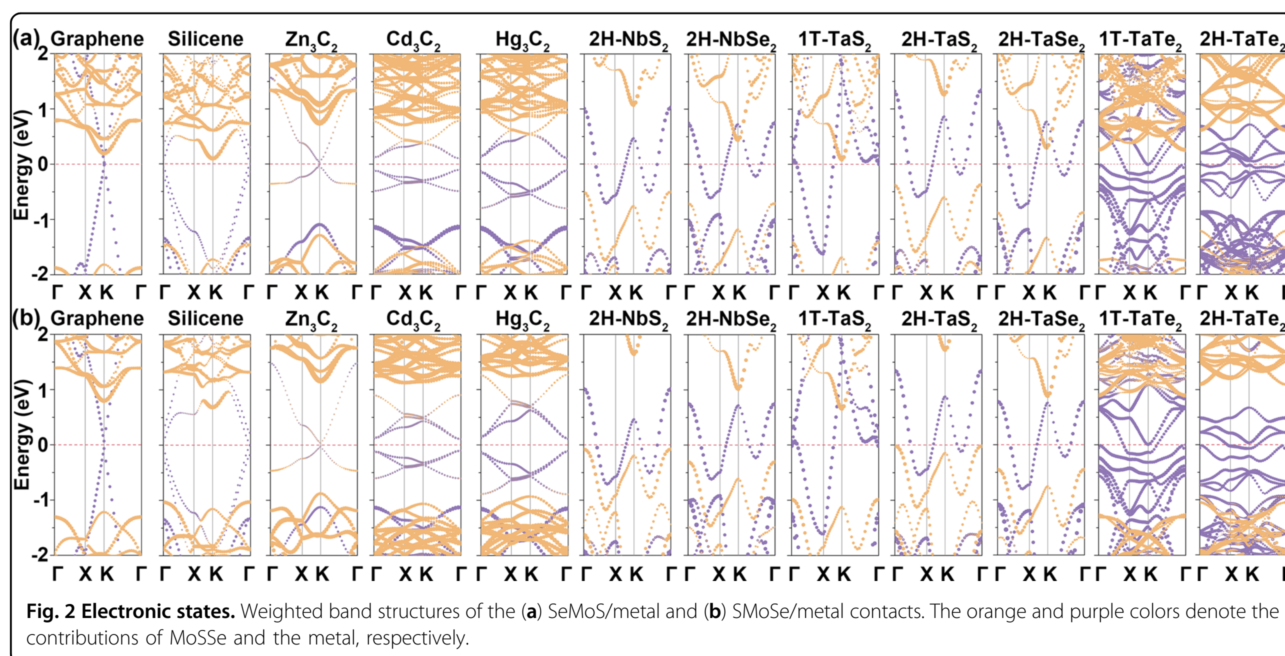

Fig. 2 Electronic states. Weighted band structures of the (**a**) SeMoS/metal and (**b**) SMoSe/metal contacts. The orange and purple colors denote the contributions of MoSSe and the metal, respectively.

the Se-side, which is consistent with previous results for the contact between MoSSe and germanene[41]. 1T-XA_2 exhibits the same trend, while 2H-XA_2 exhibits the opposite trend. As the value of d always falls within 2.9 to 3.6 Å, no chemical bonds are formed at the contact. As expected, d is smaller for the SeMoS/metal contacts than for the SMoSe/metal contacts. To enable quantitative comparison, we calculate the charge transfers Δq (Bader scheme) across the contact normalized by A, as shown in Table 1. Positive (negative) values represent forward (backward) charge transfer from the metal to MoSSe (from MoSSe to the metal). While all the values remain close to zero, the forward (backward) charge transfers at the SMoSe/metal contacts are systematically damped (enhanced) compared to the SeMoS/metal contacts.

The weighted band structures in Fig. 2a demonstrate that the SeMoS/Zn_3C_2 contact is ohmic and thus superior to the n-type SeMoS/silicene ($\Phi_n = 0.10$ eV) and SeMoS/1T-TaS_2 ($\Phi_n = 0.09$ eV) contacts, where Φ is the Schottky barrier height (SBH). While the SeMoS/Cd_3C_2 and SeMoS/Hg_3C_2 contacts develop finite band gaps (due to the sizable lattice mismatch and induced in-plane strain in these cases), the Dirac cone of the SeMoS/Zn_3C_2 contact at the Fermi level enables efficient charge transport. According to Table 1, the SeMoS/metal contacts tend to be n-type with sufficiently small SBHs. The SMoSe/Zn_3C_2 and SMoSe/2H-TaS_2 contacts are ohmic, as shown in Fig. 2b, and according to Table 1, for the other SMoSe/metal contacts, the n-type SBHs tend to be larger than the p-type SBHs. Regardless of the termination, n-type contacts are formed with the group-IV 2D metals, and ohmic contacts are formed with Zn_3C_2. In contrast, contacts with XA_2 behave differently for the two terminations, as the S-side tends to form n-type contacts and the Se-side tends to form p-type contacts.

The work functions of the considered 2D metals (W_{metal}) fall within 4.31 to 6.01 eV, and their Fermi levels (E_F) are located within the band gap of MoSSe (see the red horizontal lines in Fig. 3a). While the group-IV 2D metals and M_3C_2 have low work functions, 2H-TaS_2, 2H-NbS_2, and 2H-$NbSe_2$ are characterized by high work functions. Compared to the 2D metals, E_F changes little or shifts to higher energy (with respect to the vacuum level) for the SeMoS/metal contacts, while it shifts to lower energy for the SMoSe/metal contacts. This explains why the S-side (Se-side) tends to form n-type (p-type) contacts. For growing W_{metal}, the character of the contact evolves from n-type to p-type. In Fig. 3a, the highest occupied and lowest unoccupied states of MoSSe in the contact are marked above and below E_F (except for the Cd_3C_2/metal and Hg_3C_2/metal contacts with finite band gaps). For the ohmic contacts, only E_F is shown. Note that W_{metal} refers to the strained metals. For 2H-$NbSe_2$ and 2H-$TaSe_2$ (which exhibit a large lattice mismatch), the strain alters W_{metal} by only 0.24 and 0.23 eV, respectively, which demonstrates the robustness of our conclusions in combination with the knowledge that the band gap of MoSSe is altered by only 0.40 eV under 3% strain[42].

The SBH is very sensitive to W_{metal} according to the Schottky-Mott rule[18], which, however, is of limited validity in the case of Fermi level pinning. The pinning factor $S = |d\Phi/dW_{metal}|$ measures the shift of the Fermi level of a semiconductor/metal contact when different

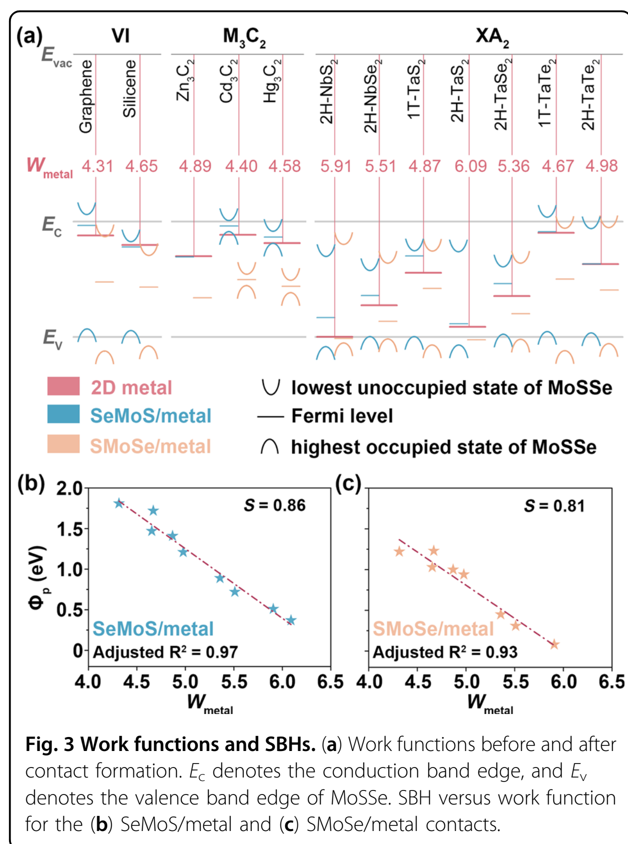

Fig. 3 Work functions and SBHs. (**a**) Work functions before and after contact formation. E_c denotes the conduction band edge, and E_v denotes the valence band edge of MoSSe. SBH versus work function for the (**b**) SeMoS/metal and (**c**) SMoSe/metal contacts.

metals are used. For $S = 0$, the Fermi level is fully pinned, while for $S = 1$, the Schottky–Mott limit is achieved. As shown in Fig. 3b, c, sizable values of $S = 0.86$ and $S = 0.81$ are obtained for contacts with the S-side and Se-side, respectively, implying that 2D metals are superior to bulk metals for contacting Janus MoSSe (even though both realize weak binding), especially for the S-side ($S = 0.28$)[43]. Due to the excellent values of S, it is expected that the Fermi level pinning will be weak.

While contacts with weak binding have the advantage of reducing the Fermi level pinning, the tunnel barrier can be an issue[44]. Figure 4a displays the electrostatic potential of the SeMoS/graphene contact with the tunnel barrier height $\Phi_{TB} = \Phi_{gap} - \Phi_{MoSSe}$ being the difference between the potential maxima of the contact (Φ_{gap}) and the termination layer of MoSSe (Φ_{MoSSe}). The tunnel barrier width W_{TB} refers to Φ_{MoSSe}. On the other hand, $\Phi_{TB} = \Phi_{gap} - \Phi_{metal}$, and W_{TB} refers to the potential minimum of the metal (Φ_{metal}) when $\Phi_{metal} > \Phi_{MoSSe}$. Low Φ_{TB} and low W_{TB}, which correspond to the bottom left corner of Fig. 4b, imply enhanced tunneling. Figure 4b indicates that there are four groups of contacts. The contacts with XA_2 constitute Groups 1 and 3, where Group 3 consists of all the contacts involving $TaTe_2$ and combines low binding energy with rather low Φ_{TB}. The contacts with group-IV 2D metals constitute Group 2, which is the least competitive. The two ohmic contacts with

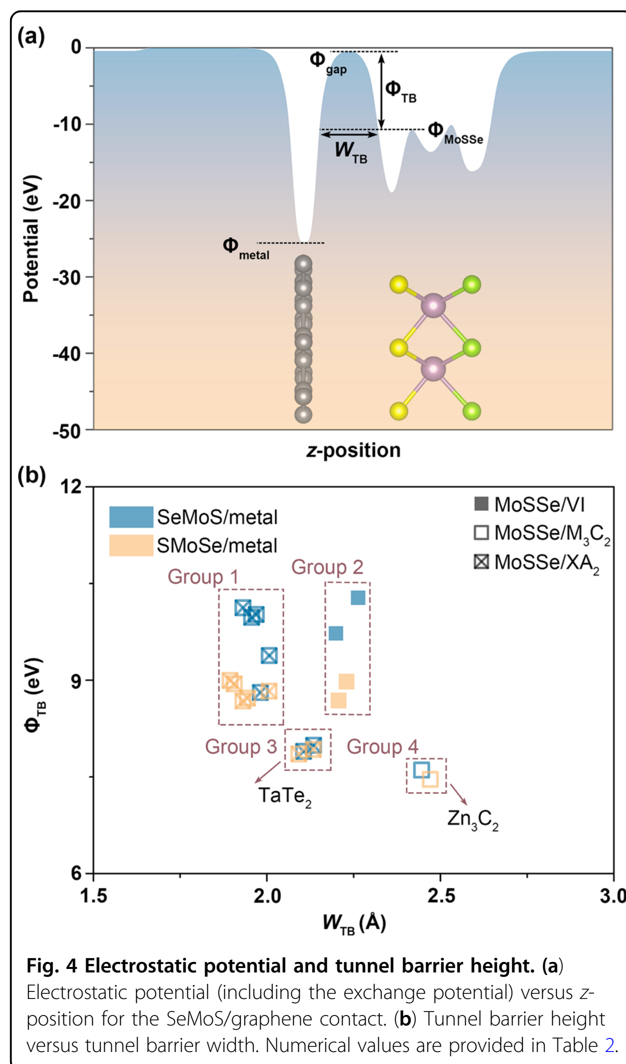

Fig. 4 Electrostatic potential and tunnel barrier height. (**a**) Electrostatic potential (including the exchange potential) versus z-position for the SeMoS/graphene contact. (**b**) Tunnel barrier height versus tunnel barrier width. Numerical values are provided in Table 2.

Zn_3C_2, which constitute Group 4, achieve the lowest Φ_{TB} but suffer from the highest W_{TB}, while the ohmic contact SMoSe/2H-TaS_2 combines low $\Phi_{TB} = 8.94$ eV with the lowest $W_{TB} = 1.91$ Å of all contacts under investigation.

Considering the inherent dipole moment of Janus materials, we next quantify the induced dipole moment of the contact. Figure 5 shows schematic diagrams of the relationship between the total dipole moment of the contact (D_{tot}) and the interfacial dipole moment (D_{int}). Two (three) classes of patterns are found for the contacts with the S-side (Se-side). The obtained values of D_{tot} and D_{int} are shown in Table 2, in which the positive (negative) sign corresponds to the direction from the 2D metal (Janus MoSSe) to Janus MoSSe (the 2D metal). D_{tot} is always negative for contacts with the S-side (classes I and II), i.e., it inherits the direction of the dipole moment of Janus MoSSe (D_{MoSSe}). Although charge transfer occurs across the contact (Table 1), the amount is not sufficient to change the direction of D_{tot}. The SeMoS/M_3C_2

contacts show the least negative values. The interfacial dipole moment $D_{\text{int}} = (D_{\text{tot}} - D_{\text{MoSSe}})/N$, where N denotes the number of unit cells of MoSSe in the supercell, may be negative (class I; D_{tot} is more negative) or positive (class II; D_{tot} is less negative). Given that D_{tot} inherits the direction of D_{MoSSe}, we expect D_{tot} to be positive for the SMoSe/metal contacts, which is true in most cases (classes III and IV). The only exceptions are the SMoSe/2H-TaS_2 and SMoSe/2H-NbS_2 contacts (class V), in which a considerable charge transfer from Janus MoSSe to the 2D metal leads to a negative D_{tot} and to a significantly negative D_{int}, resulting in a favorable ohmic behavior of the SMoSe/2H-TaS_2 contact and a tiny $\Phi_p = 0.08$ eV of the SMoSe/2H-NbS_2 contact.

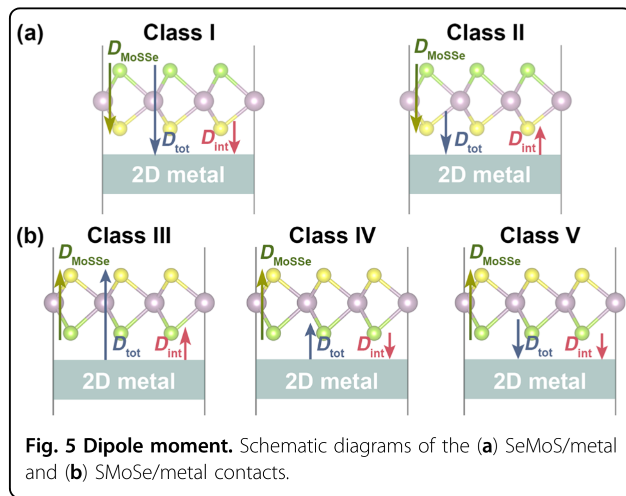

Fig. 5 Dipole moment. Schematic diagrams of the (**a**) SeMoS/metal and (**b**) SMoSe/metal contacts.

The transmission coefficient

$$T = \left(1 + \frac{\sinh^2\left(\sqrt{2m\Phi_{\text{TB}}(1-E/\Phi_{\text{TB}})}W_{\text{TB}}/\hbar\right)}{4E/\Phi_{\text{TB}}(1-E/\Phi_{\text{TB}})}\right)^{-1},$$

where E is the energy and m is the mass of the electron, is shown in Fig. 6a–d for representative contacts from the groups in Fig. 4b. In each case, $T \sim 1$ already at $E/\Phi_{\text{TB}} \lesssim 2$. Consistent with the previous discussion, T tends to be slightly higher for Se than for S termination at low energy. A comparison of the low energy range is given in Fig. 6e for the contacts with the Se-side, showing that 2H-TaS_2 and 2H-$TaSe_2$ (contacts located in the left bottom corner of Fig. 4b) result in slightly higher T. Adopting the device model of Fig. 6f, electronic transport calculations are performed for the ohmic SMoSe/2H-TaS_2 contact using channel lengths of 20.96, 26.67, and 32.67 Å. The obtained *I-V* curves in Fig. 6g demonstrate an ohmic behavior, particularly for a channel length of 20.96 Å. We use the transfer length method to extract the specific contact resistance. As the total resistance is $2R_1 + R_2$, as shown in Fig. 6f, the crossing point between the total resistance axis and the linear fit of the obtained total resistances in Fig. 6h is $2R_1$. After R_1 is multiplied with the width $w = 13.18$ Å, a specific contact resistance of 97.5 Ωμm is obtained.

Conclusions

Our first-principles study on the interaction between Janus MoSSe and various 2D metals shows that both the

Table 2 Tunnel barrier height (Φ_{TB}) and width (W_{TB}), total (D_{tot}) and interfacial (D_{int}) dipole moments, and classes of SeMoS/metal and SMoSe/metal contacts.

Metal	SeMoS/metal					SMoSe/metal				
	Φ_{TB} (eV)	W_{TB} (Å)	D_{tot} (Debye)	D_{int} (Debye)	Class	Φ_{TB} (eV)	W_{TB} (Å)	D_{tot} (Debye)	D_{int} (Debye)	Class
Graphene	10.28	2.26	−0.33	−0.09	I	8.98	2.23	0.35	0.11	III
Silicene	9.72	2.20	−0.19	0.04	II	8.68	2.21	0.31	0.08	III
Zn_3C_2	7.60	2.45	−0.18	0.05	II	7.46	2.47	0.24	0.00	III
Cd_3C_2	7.25	2.50	−0.13	0.10	II	7.21	2.60	0.30	0.07	III
Hg_3C_2	9.05	2.68	−0.19	0.04	II	8.99	2.85	0.26	0.04	III
2H-NbS_2	10.12	1.93	−0.51	−0.28	I	8.99	1.89	−0.09	−0.32	V
2H-$NbSe_2$	9.38	2.01	−0.45	−0.22	I	8.72	1.94	0.09	−0.15	IV
1T-TaS_2	10.02	1.97	−0.35	−0.12	I	8.83	2.01	0.18	−0.04	IV
2H-TaS_2	9.98	1.96	−0.44	−0.21	I	8.94	1.91	−0.03	−0.26	V
2H-$TaSe_2$	8.81	1.98	−0.40	−0.18	I	8.68	1.93	0.13	−0.09	IV
1T-$TaTe_2$	7.99	2.14	−0.21	0.01	II	7.92	2.13	0.34	0.12	III
2H-$TaTe_2$	7.90	2.11	−0.32	−0.09	I	7.86	2.09	0.28	0.05	III

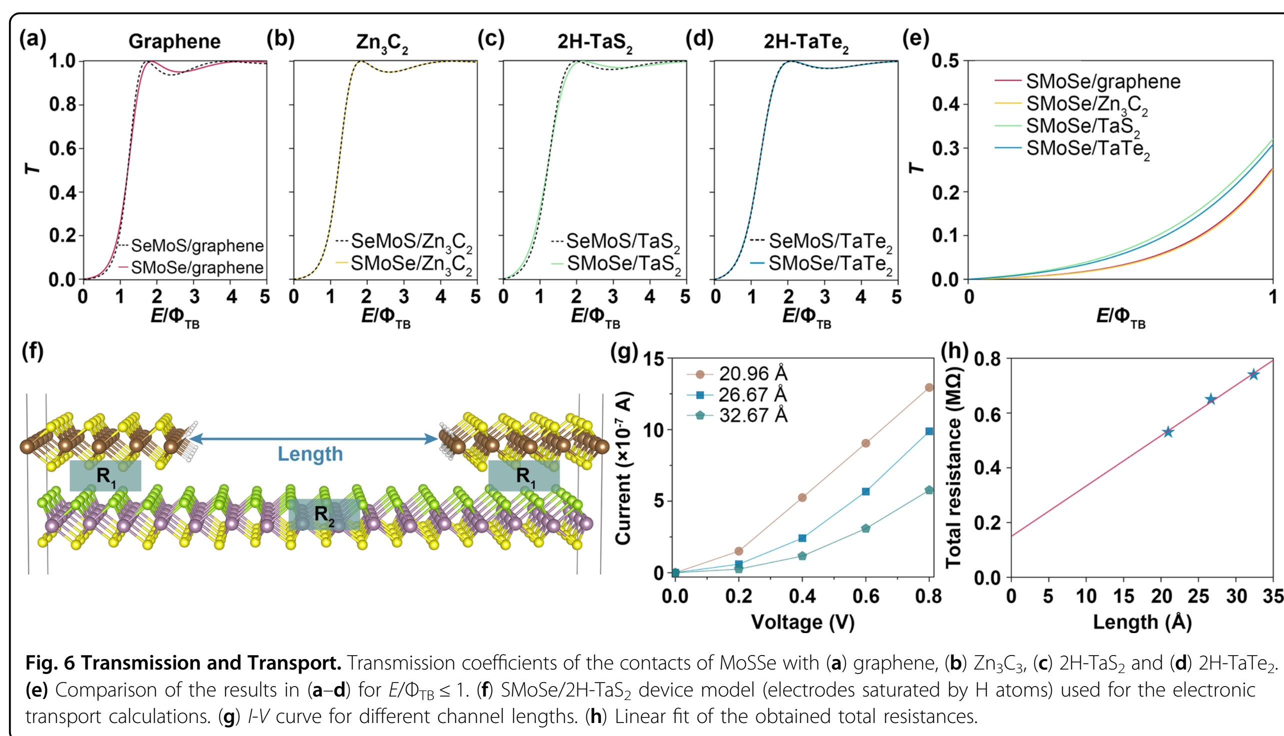

Fig. 6 Transmission and Transport. Transmission coefficients of the contacts of MoSSe with (**a**) graphene, (**b**) Zn_3C_3, (**c**) 2H-TaS_2 and (**d**) 2H-$TaTe_2$. (**e**) Comparison of the results in (**a**–**d**) for $E/\Phi_{TB} \leq 1$. (**f**) SMoSe/2H-TaS_2 device model (electrodes saturated by H atoms) used for the electronic transport calculations. (**g**) *I-V* curve for different channel lengths. (**h**) Linear fit of the obtained total resistances.

S- and Se-sides of Janus MoSSe can form ohmic contacts, as desired for electronic devices. Promising Fermi level pinning factors of 0.86 (S-side) and 0.81 (Se-side) are obtained, which reduces the Fermi level pinning. Among the studied 2D metals, Zn_3C_2 gives rise to the best contacts for both terminations of Janus MoSSe, as they are ohmic and the tunnel barriers are low (7.60 and 7.46 eV, respectively). Through its interfacial dipole moment, the SMoSe/2H-TaS_2 contact is also ohmic. Our work provides theoretical support for the application of Janus MoSSe as a channel material in nanoelectronics by identifying suitable 2D electrode materials. These 2D electrodes will not only improve the performance but also reduce the thickness of the device.

Acknowledgements
The research reported in this publication was supported by funding from King Abdullah University of Science and Technology (KAUST). This work used the computational resources of the Supercomputing Laboratory at KAUST.

Author contributions
N.Z. executed the calculations. All authors contributed to the analysis of the results and writing of the manuscript.

Data availability
Data sharing is not applicable, as no datasets were generated or analyzed.

Competing interests
The authors declare no competing interests.

Publisher's note
Springer Nature remains neutral with regard to jurisdictional claims in published maps and institutional affiliations.

Received: 19 June 2023 Revised: 8 November 2023 Accepted: 13 November 2023.
Published online: 22 December 2023

References

1. Lundstrom, M. Moore's law forever? *Science* **299**, 210–211 (2003).
2. Liu, H. et al. Phosphorene: an unexplored 2D semiconductor with a high hole mobility. *Nano Lett.* **8**, 4033–4041 (2014).
3. Wang, J. et al. High mobility MoS_2 transistor with low schottky barrier contact by using atomic thick h-BN as a tunneling layer. *Adv. Mater.* **28**, 8302–8308 (2016).
4. Zhang, H. et al. Ion gel capacitively coupled tribotronic gating for multi-parameter distance sensing. *ACS Nano* **14**, 3461–3468 (2020).
5. Fathi-Hafshejani, P. et al. Two-dimensional-material-based field-effect transistor biosensor for detecting COVID-19 Virus (SARS-CoV-2). *ACS Nano* **15**, 11461–11469 (2021).
6. Li, S.-L. et al. Quantitative Raman spectrum and reliable thickness identification for atomic layers on insulating substrates. *ACS Nano* **6**, 7381–7388 (2012).
7. Liu, C. et al. Rapid water disinfection using vertically aligned MoS_2 nanofilms and visible light. *Nat. Nanotechnol.* **11**, 1098–1104 (2016).
8. Zhang, X., Lai, Z., Ma, Q. & Zhang, H. Novel structured transition metal dichalcogenide nanosheets. *Chem. Soc. Rev.* **47**, 3301–3338 (2018).
9. Radisavljevic, B., Radenovic, A., Brivio, J., Giacometti, V. & Kis, A. Single-layer MoS_2 transistors. *Nat. Nanotechnol.* **6**, 147–150 (2011).
10. Cui, X. et al. Multi-terminal transport measurements of MoS_2 using a Van Der Waals heterostructure device platform. *Nat. Nanotechnol.* **10**, 534–540 (2015).
11. Lu, A. Y. et al. Janus monolayers of transition metal dichalcogenides. *Nat. Nanotechnol.* **12**, 744–749 (2017).
12. Yin, W. J., Wen, B., Nie, G. Z., Wei, X. L. & Liu, L. M. Tunable dipole and carrier mobility for a few layer Janus MoSSe structure. *J. Mater. Chem. C* **6**, 1693–1700 (2018).

13. Zhang, K. et al. Enhancement of Van Der Waals interlayer coupling through polar Janus MoSSe. *J. Am. Chem. Soc.* **142**, 17499–17507 (2020).
14. Liu, J. et al. Asymmtric schottky contacts in Van Der Waals metal-semiconductor-metal structures based on two-dimensional Janus materials. *Research* **2020**, 6727524 (2020).
15. Fan, Z.-Q., Zhang, Z.-H. & Yang, S.-Y. High-performance 5.1 nm in-plane Janus WSeTe Schottky barrier field effect transistors. *Nanoscale* **12**, 21750–21756 (2020).
16. Brillson, L. J. The structure and properties of metal-semiconductor interfaces. *Surf. Sci. Rep.* **2**, 123–326 (1982).
17. Palsgaard, M., Gunst, T., Markussen, T., Thygesen, K. S. & Brandbyge, M. Stacked Janus device concepts: abrupt pn-junctions and cross-plane channels. *Nano Lett.* **18**, 7275–7281 (2018).
18. Bardeen, J. Surface states and rectification at a metal semiconductor contact. *Phys. Rev.* **71**, 717–727 (1947).
19. Mead, C. A. Metal-semiconductor surface barriers. *Solid State Electron* **9**, 1923–1033 (1966).
20. Kim, C. et al. Fermi level pinning at electrical metal contacts of monolayer molybdenum dichalcogenides. *ACS Nano* **11**, 1588–1596 (2017).
21. Liu, Y. et al. Approaching the Schottky-Mott limit in Van Der Waals metal-semiconductor junctions. *Nature* **557**, 696–700 (2018).
22. Wang, Y. et al. Van Der Waals contacts between three-dimensional metals and two-dimensional semiconductors. *Nature* **568**, 70–74 (2019).
23. Chuang, S. et al. MoS_2 p-type transistors and diodes enabled by high work function MoO_x contacts. *Nano Lett.* **14**, 1337–1342 (2014).
24. Farmanbar, M. & Brocks, G. Ohmic contacts to 2D semiconductors through Van Der Waals bonding. *Adv. Electron. Mater.* **2**, 1500405 (2016).
25. Shi, Y. et al. Work function engineering of graphene electrode via chemical doping. *ACS Nano* **4**, 2689–2694 (2010).
26. Wang, G., Kim, Y., Choe, M., Kim, T.-W. & Lee, T. A new approach for molecular electronic junctions with a multilayer graphene electrode. *Adv. Mater.* **23**, 755–760 (2011).
27. Britnell, L. et al. Field-effect tunneling transistor based on vertical graphene heterostructures. *Science* **335**, 947–950 (2012).
28. Zhang, J. et al. SWCNT-MoS_2-SWCNT vertical point heterostructures. *Adv. Mater.* **29**, 1604469 (2017).
29. Shen, T., Ren, J.-C., Liu, X., Li, S. & Liu, W. Van Der Waals stacking induced transition from Schottky to ohmic contacts: 2D metals on multilayer InSe. *J. Am. Chem. Soc.* **141**, 3110–3115 (2019).
30. Shen, T. et al. Electric field screening in gate-tunable Van Der Waals 2D-metal/InSe junctions. *Adv. Funct. Mater.* **32**, 2207018 (2022).
31. Mishchenko, A. et al. Twist-controlled resonant tunnelling in graphene/boron nitride/graphene heterostructures. *Nat. Nanotechnol.* **9**, 808–013 (2014).
32. Campbell, P. M., Tarasov, A., Joiner, C. A., Ready, W. J. & Vogel, E. M. Enhanced resonant tunneling in symmetric 2D semiconductor vertical heterostructure transistors. *ACS Nano* **9**, 5000–5008 (2015).
33. Zhang, P. et al. Epitaxial growth of metal-semiconductor Van Der Waals heterostructures NbS_2/MoS_2 with enhanced performance of transistors and photodetectors. *Sci. China Mater.* **63**, 1548–1559 (2020).
34. Kresse, G. Efficient iterative schemes for ab initio total-energy calculations using a plane-wave basis set. *Phys. Rev. B* **54**, 11169–11186 (1996).
35. Thonhauser, T. et al. Van Der Waals density functional: self-consistent potential and the nature of the Van Der Waals bond. *Phys. Rev. B* **76**, 125112 (2007).
36. Liu, J., Shen, T., Ren, J.-C., Li, S. & Liu, W. Role of Van Der Waals interactions on the binding energies of 2D transition-metal-dichalcogenides. *Appl. Surf. Sci.* **608**, 155163 (2023).
37. Bjorkman, T. Testing several recent Van Der Waals density functionals for layered. *Struct. J. Chem. Phys.* **141**, 074708 (2014).
38. Heyd, J., Scuseria, G. E. & Ernzerhof, M. Screened hybrid density functionals applied to solids. *J. Chem. Phys.* **124**, 219906 (2006).
39. Smidstrup, S. et al. First-principles Green's-function method for surface calculations: a pseudopotential localized basis set approach. *Phys. Rev. B* **96**, 195309 (2017).
40. Liu, P.-F., Zhou, L., Tretiak, S. & Wu, L.-M. Two-dimensional hexagonal M_3C_2 (M = Zn, Cd and Hg) monolayer: novel quantum spin hall insulators and Dirac cone materials. *J. Mater. Chem. C* **5**, 9181–9187 (2017).
41. Zhao, N. & Schwingenschlögl, U. Transition from Schottky to ohmic contacts in Janus MoSSe/germanene heterostructures. *Nanoscale* **12**, 11448–11454 (2020).
42. Riis-Hensen, A. C., Manti, S. & Thygesen, K. S. Engineering atomically sharp potential steps and band alignment at solid interfaces using 2D Janus layers. *J. Phys. Chem. C* **124**, 9572–9580 (2020).
43. Zhao, N. & Schwingenschlögl, U. Dipole-induced ohmic contacts between monolayer Janus MoSSe and bulk metals. *NPJ 2D Mater. Appl.* **5**, 72 (2021).
44. Allain, A., Kang, J., Banerjee, K. & Kis, A. Electrical contact to two-dimensional semiconductors. *Nat. Mater.* **14**, 1195–1205 (2015).